

Hanle diagnostics of solar magnetic fields: the Sr II 4078 Å line

M. Bianda¹, J.O. Stenflo², and S.K. Solanki²

¹ Istituto Ricerche Solari Locarno (IRSOL), Via Patocchi, CH-6605 Locarno-Monti, Switzerland

² Institute of Astronomy, ETH Zentrum, CH-8092 Zürich, Switzerland

Received 1 April 1998 / Accepted 18 May 1998

Abstract. The Hanle depolarization and rotation effects in the Sr II 4078 Å line have been explored with the instrumentation at IRSOL (Istituto Ricerche Solari Locarno) by recording the Stokes I , Q , and U line profiles with high spectral resolution and polarimetric accuracy in a large number of regions across the solar disk. From the extracted line parameters we have constructed “Hanle histograms” showing the statistical distributions of the Hanle rotation and depolarization effects. Comparison with theoretical calculations allow these histograms to be understood in terms of magnetic fields with a strength of about 5–10 G, which is similar to the field strengths previously found through analysis of Q/I Hanle depolarization in the Ca I 4227 Å line. While small-scale magnetic fields with spatially unresolved angular distributions contribute to the observed Hanle depolarization effects, the observed Hanle rotation effects in Stokes U are due to spatially resolved fields with net large-scale orientations (e.g. global or canopy-type fields). We have also for the first time determined empirical “Hanle efficiency profiles”, derived independently for the Hanle rotation and depolarization effects. They show how the Hanle efficiency has its maximum in the Doppler core of the line and then rapidly decreases to become zero in the line wings.

Key words: polarization – scattering – Sun: magnetic fields – atomic processes – techniques: polarimetric

1. Introduction

The Hanle effect allows magnetic-field diagnostics in a parameter domain that is not well accessible to the usual Zeeman effect. It therefore provides us with a new window for the exploration of solar magnetism, e.g. of weak magnetic fields, turbulent fields, and chromospheric canopy fields (cf. Stenflo 1994). Only through the recent development of highly sensitive imaging polarimeters has it become possible to take full advantage of the Hanle effect, e.g. with ZIMPOL (Zurich Imaging Polarimeter) (Povel 1995; Stenflo et al. 1998) and with the polarimeter at IRSOL (Istituto Ricerche Solari Locarno) (Bianda et al. 1998).

The Hanle effect modifies the polarization that is produced by coherent scattering in spectral lines. This modification manifests itself in two ways, as depolarization, and as rotation of

the plane of linear polarization. In a recent paper (Bianda et al. 1998, here referred to as Paper I) we have explored the spatial fluctuations of the Hanle depolarization across the solar disk in the Ca I 4227 Å line with the new polarimeter system at IRSOL. The Ca I 4227 Å line is a normal Zeeman triplet and possesses the largest polarization amplitude in the entire visible solar spectrum (Stenflo et al 1983a,b). It has a linear polarization profile with three maxima, one in the Doppler core, and one in each of the blue and red line wings. The Hanle effect only operates in the Doppler core and is absent in the wings (cf. Stenflo 1994, pp. 82–83). Because of this property it was possible through observations of only two Stokes parameters (I and Q) to statistically identify the signature of Hanle depolarization and exploit it for field-strength determinations.

Since the diagnostic possibilities with the Hanle effect are based on complex physical processes with subtle observational effects, which have only begun to be explored, it is of great value to extend the observational domain by using different spectral lines that respond differently to the Hanle effect, and to observe both Stokes Q and U rather than only Q alone, so that both the Hanle depolarization and rotation effects can be recorded. This allows us to better constrain the theoretical interpretations and in particular to check the consistency and uniqueness of the Hanle interpretation, and to explore how the Hanle effect manifests itself in practice.

In the present paper we explore the Hanle effect in the Sr II 4078 Å line. From early surveys of the scattering polarization throughout the solar spectrum (Stenflo et al. 1980, 1983a,b) it has been known that this line belongs to the more strongly polarizing ones, but it has never before been used for Hanle analysis. In contrast to the Ca I 4227 Å line it is not a normal triplet but a $J = \frac{1}{2} \rightarrow \frac{3}{2} \rightarrow \frac{1}{2}$ scattering transition, similar to the Na I D₂ 5889 Å line (if we disregard the hyperfine structure and associated lower-level atomic polarization of that line, cf. Landi Degl’Innocenti 1998). Its intrinsic polarizability, represented by the factor W_2 , is 0.5 (in contrast to 1.0 for the Ca I 4227 Å line), which means that half of the scattering processes occur as classical dipole scattering, while the other half occurs as isotropic, unpolarized scattering. Like the Ca I 4227 Å line the Sr II 4078 Å polarization profile has three peaks, one core and two wing peaks, but in the case of Sr II the wing peaks lie much closer to the core peak, which means that the Hanle effect

may not be entirely absent although greatly suppressed in these wings.

In comparison with Paper I we have in the present paper extended the Hanle diagnostics by observing the three Stokes parameters I , Q , and U (the fourth, Stokes V , was also observed but is not analysed further here), rather than only I and Q , so that we can make simultaneous use of both the Hanle depolarization and rotation effects, explore the relation between them and their statistical distributions, as well as the profile variations of these effects across the core and wing peaks. This significantly extends our insight into the workings of the Hanle effect, and it places the Hanle interpretations on firmer ground. The results on the magnetic field strengths from this more complete Hanle diagnostic in the Sr II line can then be compared with the more limited diagnostic used in our previous Ca I analysis.

2. Observational technique

As in Paper I all our observations have been carried out with the Gregory-Coudé telescope, Czerny-Turner spectrograph, and polarizing beam splitter at IRSOL (Istituto Ricerche Solari Locarno) in Switzerland. The polarizer, a polarizing calcite beam splitter system, has been upgraded to allow the recording of all four Stokes parameters. This polarimeter is placed immediately in front of the spectrograph entrance slit, producing two images in orthogonal polarization states, which are then simultaneously recorded by the UV sensitive CCD camera in the spectrograph focal plane. With four settings of a $\lambda/2$ plate in front of the calcite beam splitter, four image pairs are recorded sequentially: $I \pm Q$, $I \mp Q$, $I \pm U$, and $I \mp U$. The $\lambda/2$ plate can be rapidly replaced by a $\lambda/4$ plate, and two settings of this plate gives us the image pairs $I \pm V$ and $I \mp V$.

Two image pairs, i.e., four images, are thus needed to extract each of the Stokes Q , U , and V parameters. This allows us to eliminate the two main noise sources: seeing noise and gain-table noise. The two images in one image pair have identical seeing distortions but different gain tables. For the second image pair the polarization signals have changed sign (which is as if the two images have traded places, and we have exchanged the gain tables), but the seeing has also changed. By forming ratios between the four images in a certain way, as described in great detail in Paper I (cf. also Semel et al. 1993; Semel 1995), we can extract an image of the fractional polarization (Q/I , U/I , or V/I) that is free from both seeing noise and gain-table noise. In this way we have been able to obtain polarized spectra with noise levels approaching 10^{-4} in the fractional polarization. For details we refer to Paper I.

The alignment of the beam splitter and the CCD has been done as described in Paper I. The position angles for the four settings of the $\lambda/2$ plate and the two settings of the $\lambda/4$ plate have been carefully calibrated with linear and circular polarizers. During the observations the positioning of the wave plate to the fixed, pre-calibrated positions, is done manually between the image pair exposures, while the CCD frame is transferred to the PC (which takes about 5 s), or while the frames are stored on hard disk (which takes about 15 s).

A new feature of the present observations is the use of a 1-D seeing corrector in the form of a rapidly tilting plate. It eliminates image motions, mechanical drifts, and declination changes of the Sun in a direction perpendicular to the nearest solar limb. In this way the spectrograph slit, which is always aligned parallel to the nearest solar limb, can be kept at a constant and well defined limb distance during the observations. This greatly reduces the observational uncertainty in μ ($= \cos \theta$), which was a significant source of scatter in the Ca I observations of Paper I.

This image corrector represents an upgrade of an instrument proposed by E. Wiehr and described by Sütterlin et al. (1997). A 45° mirror in front of the calcite beam splitter intercepts a portion of the solar limb just below the beam that enters the spectrograph and is used for the polarimetry. The intercepted portion of the beam is directed through the tilting glass plate to a diode array that senses the position of the solar limb. A servo stepping motor tilts the glass plate to maintain a constant limb position on the diodes. A second glass plate, which is placed between the polarizing beam splitter and the spectrograph slit, is tilted in synchrony with the first glass plate. Since this second plate is located after the polarization optics, it introduces no instrumental polarization. As the two limb portions used for the observations and for the first servo plate are separated from each other by about 30 arcsec along the limb, the seeing is not identical in the two beams, but the largest-amplitude image motions should still be similar in the two beams. This is verified by the practical application of the system, since it brings us a major improvement in the positioning and stability of the portion of the solar limb at which we observe.

If we disregard the instrumental polarization introduced by the vacuum entrance window, the telescope is polarization free during the time of the spring or fall equinox. Our present observations have been carried out on March 18, 19, 20, 21, and 26, near the spring 1997 equinox. We have collected 126 Q/I , 112 U/I , and 91 V/I measurements of the Sr II 4078 Å line. Each image covers about 15 arcsec in the spatial direction and the interval 4077.2 – 4078.8 Å in the spectral direction. This interval includes the line and a portion around 4078.7 Å that is close to the continuum level. This portion aids us in determining the precise limb distance or μ position (see below).

The spectrograph slit was always placed parallel to the nearest solar limb. Stokes Q is defined to be positive along the limb direction. The 1-D image corrector system was used only when observing near the extreme limb, for $\mu < 0.3$. Since no image rotator was used, our choice of limb position was limited in the same way as in Paper I. Typical exposure times near the limb were 15–30 s.

As described in Paper I, the noise is not only random but contains a fixed-pattern background in the fractional polarization. This background, in the form of an irregular, wavelength-dependent zero-line offset, is determined by making alternating recordings near the limb (for the actual measurements) and at disk center (for the fixed-pattern calibrations), and subtracting the disk-center Q/I , U/I , or V/I data from the corresponding limb data. At disk center the intrinsically solar scattering polar-

ization vanishes for symmetry reasons, while the spurious background that affects the limb observations remains unchanged. Typically one disk-center calibration was carried out for every five limb observations.

3. Data reduction

The main steps in the data reduction are the following: (1) Dark current subtraction; (2) Determination of μ (or the precise limb distance); (3) Flat fielding (only required for Stokes I); (4) Extraction of the fractional polarizations Q/I and U/I ; (5) Determination and removal of stray light; (6) Correction for the varying zero-line offset of the fractional polarization; (7) Removal of $Q \rightarrow U$ instrumental cross talk; (8) Fourier smoothing for noise suppression. As most of these steps have been explained in detail in Paper I, we only comment here on new aspects that have not been discussed before.

To determine the precise μ value we make use of the measurements of the mean intensity (after dark current subtraction) around 4078.7 Å in our spectra, where the intensity is expected to be 0.956 in units of the local continuum intensity. Regular measurements at disk center allow us to follow and interpolate variations in the sky transparency, so that the limb intensities can be expressed in units of the disk center intensity. From these values a μ position can be obtained, using the earlier determinations of the center-to-limb intensity variations by Pierce & Slaughter (1977).

As in Paper I the Stokes I line profiles at disk center could be used to determine the amount of spectrograph stray light by comparison with corresponding FTS profiles from Kitt Peak obtained by H. Neckel. Values between 1.0 and 1.5% were found and used to correct the polarization data (assuming that the stray light is unpolarized).

As already mentioned, the fixed-pattern noise or wavelength-dependent zero-line offset was calibrated by the disk-center observations and then subtracted from the data. Special care had to be taken to avoid the influence of magnetic regions in the disk-center recordings. The fixed-pattern background had the same structure in both Q/I and U/I , and it was for the Sr II 4078 Å line similar to that of the Ca I 4227 Å line. All these observations used the same $\lambda/2$ plate. In the case of the circular polarization measurements (V/I), however, for which the $\lambda/2$ plate is replaced by a $\lambda/4$ plate, the fixed pattern is practically zero. This indicates that the source of the fixed pattern is in the $\lambda/2$ plate, but as it is reproducible, it can be removed from the data.

After the fixed pattern has been removed, the near-limb continuum polarization was often far from zero, as expected for Q/I due to intrinsic solar continuum polarization. Although after the fixed-pattern removal the background is spectrally flat, we do not believe that it represents the true zero point of the polarization scale, so we add a constant zero-line shift to the data, determined in the following way: Within each interval of μ we require that all recorded Q/I profiles should have the same polarization amplitude in the farthest portions of the line wings, as close to the continuum as possible, since it is reasonable

to assume that the continuum polarization is only a function of limb distance or μ . Next we inspect the Q/I profile shapes of the depolarizing blend lines in the line wings and require their relative shapes and depths to match as closely as possible the corresponding relative shapes and depths of the Stokes I blend profiles. There is an element of subjective judgement in this procedure, which introduces some uncertainty, but no better procedure exists at present (cf. the discussion in Stenflo et al. 1998). All this uncertainty however does not significantly affect our determinations of relative line polarization amplitudes and Hanle depolarizations.

We find substantial $Q \rightarrow U$, V and $U \rightarrow V$ cross talk in our observations, which most probably originates from stresses in the vacuum entrance window of the telescope, since the polarization of the two mirror reflections should cancel each other at the time of the equinox. Imperfections and misalignment of the $\lambda/2$ plate may also contribute to the cross talk. Since we are not studying Stokes V in the present paper, and infiltration of Stokes V (from the longitudinal Zeeman effect) into Q and U is insignificant in our data (it would be recognized by the spatially structured anti-symmetric line profile signatures), we are here only concerned with cross talk between Q and U .

The dominant $Q \rightarrow U$ cross talk can be easily identified, since the U polarization is exclusively produced by Hanle rotation and only occurs in the Doppler core, while Q/I has strong non-magnetic polarization in the line wings. $Q \rightarrow U$ cross talk can then be eliminated by subtracting from the observed U/I a certain fraction of the observed Q/I , determined by the requirement that the corrected U/I profile should be zero in the distant line wings. Application of this method leads to both positive and negative Stokes U/I profiles, as expected, since the Hanle rotation can have both signs. A sign change can happen in recordings taken only few minutes apart in different solar regions. In this case subtraction of the same amount of cross talk gives very consistent results, which supports the validity of the method.

$U \rightarrow Q$ cross talk cannot be identified so readily in the data, since Q/I has large and variable polarization in the Doppler core, where a spurious U/I contribution may be present. However, since the intrinsic U/I amplitude (which is exclusively due to the Hanle effect) is much smaller than the Q/I amplitude in the majority of the cases (cf. Fig. 7a and b below), the $U \rightarrow Q$ cross talk will not be a very serious problem, although it will introduce some additional noise (of both signs) in the Q/I core polarization. Note that this additional noise only occurs if Hanle rotation is present.

4. Analysis and results

4.1. The Stokes I , Q/I , and U/I profiles

Fig. 1a shows a typical disk center profile of Stokes I (normalized to the intensity I_c of the local continuum). It can be compared with the near-limb profiles in Fig. 1b, at $\mu = 0.1$ (dotted line), $\mu = 0.25$ (dashed line), and the average of the recorded profiles in the interval $0.1 \leq \mu \leq 0.25$ (solid line).

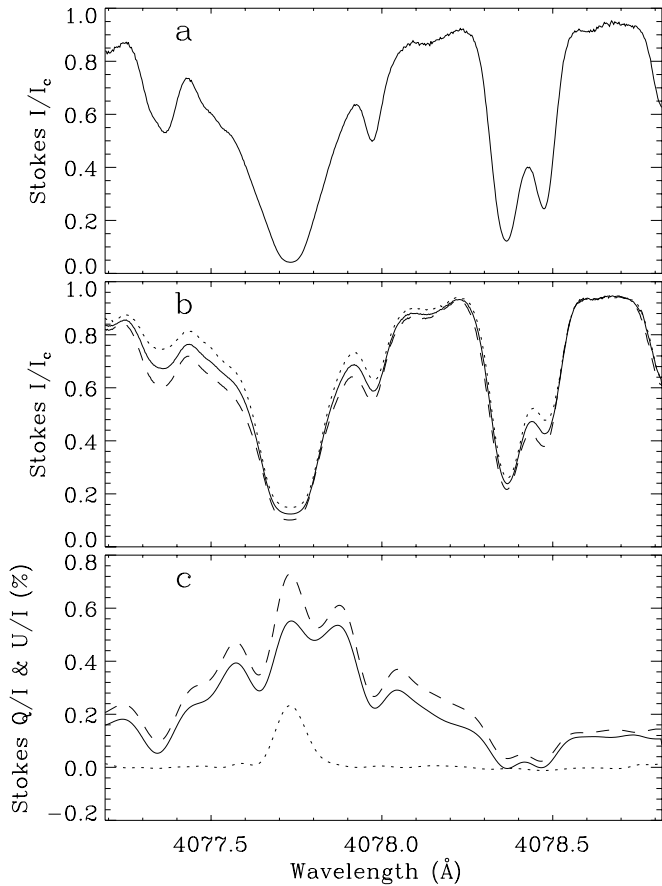


Fig. 1a–c. Stokes I , Q , and U line profiles of the Sr II 4078 Å line. **a** Stokes I at disk center, normalized to the intensity I_c of the local continuum. **b** Stokes I/I_c near the solar limb. Dotted line: $\mu = 0.1$. Dashed line: $\mu = 0.25$. Solid line: Average of all the profiles recorded within $0.1 \leq \mu \leq 0.25$. **c** Dotted line: Average of all the Stokes U/I profiles with an amplitude exceeding 0.08 %. Solid line: Average of the Stokes Q/I profiles for the same sample of solar regions as used for the mean U/I . Dashed Line: Average of all the Stokes Q/I profiles, for which the corresponding U/I profile had an amplitude less than 0.08 %.

All the profiles have been normalized to 0.95 at 4078.7 Å (since no clear continuum is reached). Note the disappearance of the lanthanum blend line at 4077.36 Å as we approach the limb.

In Fig. 1c we have plotted averages of the Q/I (solid and dashed lines) and U/I (dotted line) profiles recorded in the interval $0.1 \leq \mu \leq 0.25$. Since many individual U/I spectra did not show significant signals above the noise level, we have when forming the U/I average in Fig. 1c only selected the profiles with a U/I amplitude greater than 0.08 %, a total of 16 profiles. Before averaging, the U/I profiles have been multiplied by either +1 or -1 to ensure that all the averaged profiles have a positive polarization amplitude in the line core. The corresponding mean Q/I profile for this sample of 16 recordings is represented by the solid line. In the considered $0.1 \leq \mu \leq 0.25$ interval 46 recordings had a U/I amplitude below 0.08 %. The mean Q/I profile for these 46 recordings is given by the dashed line. The average μ value for this sample of 46 recordings is slightly

smaller (0.16) than for the sample of 16 recordings (0.19). This may contribute somewhat to the systematically larger polarizations of the dashed curve.

We notice that the Q/I profiles of the Sr II line have a triplet structure (disregarding the influence of the blend lines): A polarization peak in the Doppler core as well as peaks in the blue and red line wings. This is qualitatively similar to the behavior of the Ca I 4227 Å line, except that the wing peaks are much closer to the core in the case of Sr II (about 0.15 Å as compared with about 0.5 Å for Ca I). The Q/I profile is also locally depolarized by blend lines at 4077.36, 4077.97, 4078.36, and 4078.47 Å.

The mean U/I profile in Fig. 1c only exhibits a single peak in the Doppler core of the line and is zero outside. This is expected as U/I is exclusively due to the Hanle rotation effect, which only operates in the Doppler core and is absent in the wings (cf. Stenflo 1994, pp.82–83).

Fig. 2a–d illustrates how the individual polarization profiles may vary from place to place on the Sun (each place representing a spatial average of 15 arcsec along the slit). Thus Fig. 2a shows a strong Q/I core peak while U/I remains small, Fig. 2b shows a combination of strong Q/I and U/I core peaks, Fig. 2c a greatly suppressed Q/I core peak together with the absence of a U/I signal, Fig. 2d a suppressed Q/I peak in combination with a strong U/I peak. This demonstrates how the Hanle depolarization, which only occurs in the Q/I Doppler core, can vary greatly across the solar surface, with or without an accompanying Hanle rotation (represented by U/I). There is thus no simple correlation between Hanle depolarization and rotation. The relation between them will be elucidated later in connection with histograms showing the distribution of these effects.

4.2. Behavior of the Q/I wing and core maxima

Like in Paper I for Ca I we explore the relative behavior of the Q/I maxima in the blue wing, line core, and red wing. In comparison with the Ca I case, the blue and red wing maxima lie much closer to the core for Sr II: 160 and 150 mÅ as compared with 500 and 400 mÅ for Ca I. Some Q/I profiles (about 10 % of them) have no well-defined maxima, e.g. Fig. 2b in the blue wing, and Fig. 2d in the line core. In these cases we have simply extracted the Q/I value at the wavelength where the maximum is otherwise supposed to be.

Fig. 3a–c illustrates the behavior of the CLV (center-to-limb variation) of the three Q/I maxima. When we compare Fig. 3a with the corresponding Fig. 2a in Paper I for Ca I, we notice that the spread of the points at small μ values, in particular for $0.05 \leq \mu \leq 0.2$, is smaller for Sr II. This is largely the result of our present use of a 1-D image stabilizer and better determination of the μ position, as described in Sects. 2 and 3. The solid curve in Fig. 3a represents a fit with a function of the form

$$Q/I = \frac{a(1 - \mu^2)}{\mu + b}, \quad (1)$$

first introduced by Stenflo et al. (1997). The fit in Fig. 3a has been obtained with $a = 0.16$ % and $b = 0.095$.

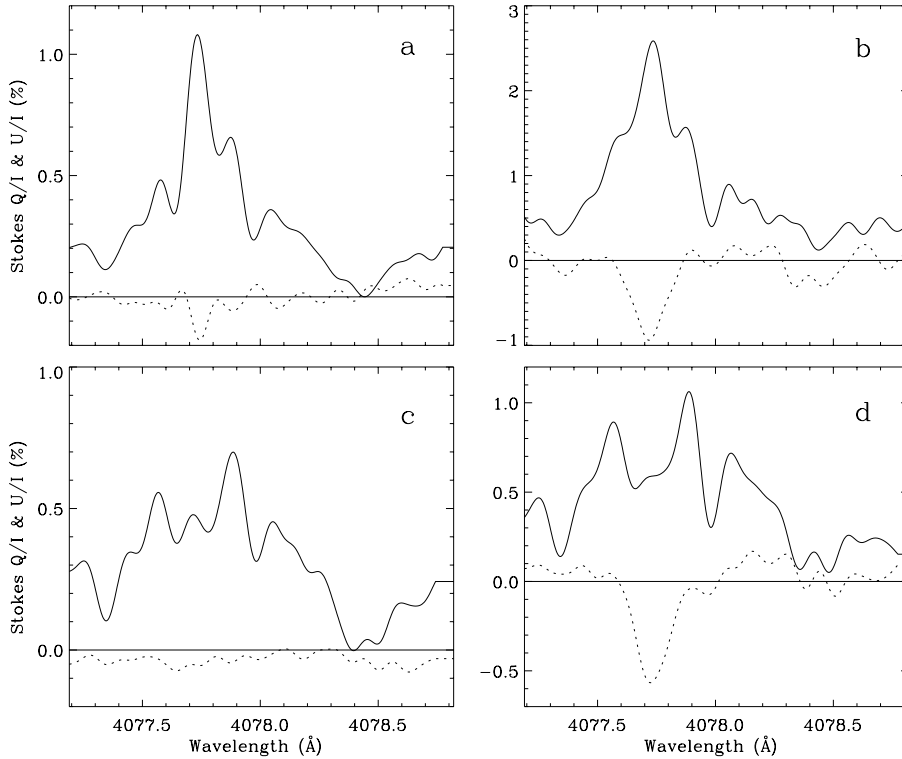


Fig. 2a–d. Examples of variations in the Stokes Q/I (solid curves) and U/I (dotted curves) line profiles due to variable Hanle depolarization and rotation. Note that these variations occur almost exclusively in the line core. In **b** and **a** we see strong Q/I core peaks both with and without a strong U/I signature, while in **d** and **c** we see that the near absence of a Q/I core peak can be accompanied by a U/I spectrum that both does or does not have a strong U/I signal.

The solid curve in Fig. 3b for the red wing has been derived by combining the curve for the blue wing in Fig. 3a and the second-order polynomial fit of the relation between the red and blue wings in Fig. 4a (see below).

In contrast to the well-defined CLV relations for the line wings, the line-center data in Fig. 3c exhibit a large scatter which, like in the Ca I case, can be naturally understood in terms of spatially varying Hanle depolarization, since such magnetic-field effects only affect the core but not the wings. In the absence of magnetic fields we would expect the spread in the core to be the same as that in the wings. Using the functional form (1) with different values for the a and b parameters, we have plotted in Fig. 3c two different “envelope curves”, which are supposed to represent our estimate of what the line-center CLV curve would be in the absence of magnetic fields, for vanishing Hanle depolarization. If there were no observational errors, we would for small values of μ (see Fig. 11 below for a discussion of the larger μ values) expect practically all observed points to fall below the envelope curve. This is approximately the case for the dotted curve. Since however we do have observational scatter, we need to allow for the possibility that some points may fall on the “wrong” side of the envelope. The dashed curve in Fig. 3c represents the lowest possible choice for a non-magnetic envelope that would still be consistent with the Hanle interpretation and the observational scatter. Although there is thus a lowest envelope choice, there is in principle no direct upper bound on the choice. A higher choice of envelope however implies larger Hanle depolarizations and thus larger field strengths.

The relations between the red and blue wing polarizations Q_r/I and Q_b/I are given in Figs. 4a and 5, while Fig. 4b gives

the relation between the line center and the blue wing. Figs. 4a and 5 show that the relation between the polarizations in the two line wings is not linear, in contrast to our results for Ca I (cf. Fig. 3a in Paper I). This can be understood in terms of a difference in the CLV of the blend lines in the blue and red line wings. As the blend in the blue wing is stronger than in the red wing and weakens towards the limb (cf. Fig. 1a–c), the Q_r/Q_b ratio will decrease towards the limb, which can account for the curvature in Fig. 4a and the slope of the dotted line in Fig. 5.

The standard deviation of the points around the solid curve in Fig. 4a, which represents a second-order polynomial fit to the data, is found to be 0.075%. This may be compared with the value 0.034% for the corresponding scatter of the Ca I data within the interval $0 < Q/I < 2\%$ in Fig. 3a of Paper I. Approximately the same value of 0.075% is obtained as the instrumental noise directly from the individual Q/I and U/I profiles when the Fourier smoothed profiles are subtracted from the raw profiles and the standard deviation is calculated. From this value for the instrumental noise in Q/I we can then derive the standard deviation in the Q_r/Q_b ratio of Fig. 5, σ_{Q_r/Q_b} . In Fig. 5 the dotted line represents a linear fit to the data, while the solid curves are obtained when we add and subtract σ_{Q_r/Q_b} to this fit.

The much larger scatter of the points in Fig. 4b is interpreted as in Paper I in terms of Hanle depolarization. The dotted and dashed curves have been obtained from the corresponding envelope curves in Fig. 3c in combination with the blue-wing fit curve of Fig. 3a. They are supposed to represent two estimates of the relation between the line center and the blue wing in the

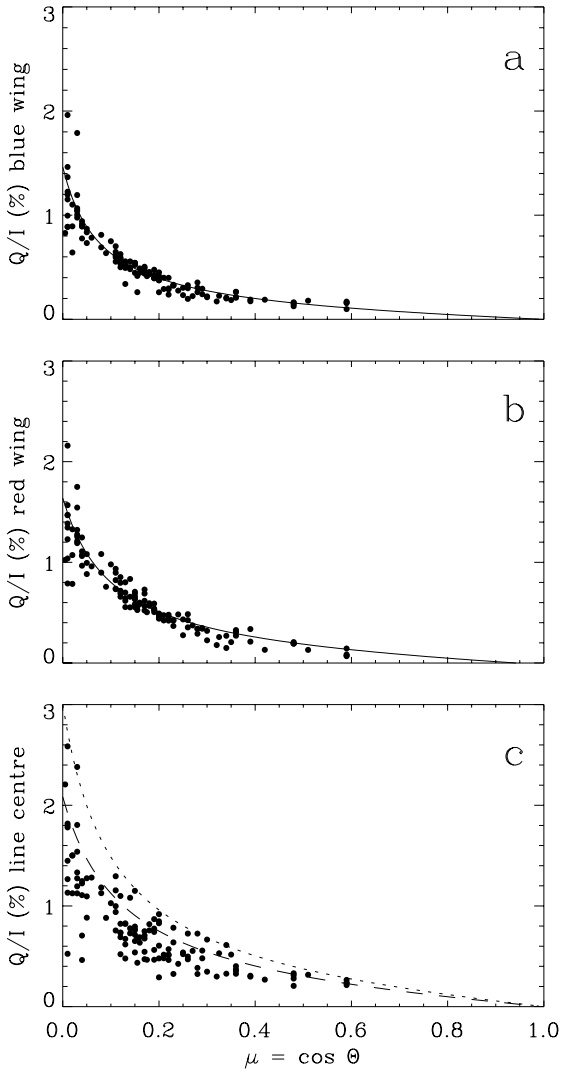


Fig. 3a–c. Center-to-limb variations of the Q/I maxima in the **a** blue line wing, **b** red wing, and **c** line center. The solid line in **a** represents a fit with the analytical function of Eq. (1), using the values $a = 0.16\%$ and $b = 0.095$ for the free parameters. The solid line in (b) is obtained from a combination of the fit function used for **a** and the second-order polynomial fit in Fig. 4a. The dotted and dashed curves in **c** represent estimated envelopes (later referred to as env. 1 and env. 2, respectively) to the data points, using the analytical function of Eq. (1) with different values for the two free parameters.

absence of magnetic fields. We notice that the dotted curve is more nearly linear than the dashed curve.

We use Fig. 4b to calculate the amount of Hanle depolarization rather than Fig. 3c, since the ratios between the points and the envelopes are affected by the μ uncertainties in Fig. 3c, while this is not the case in Fig. 4b. Fig. 6a and b shows the results obtained when forming these line center / envelope ratios from the data in Fig. 4b. Fig. 6a is based on the dotted envelope curve (env. 1), Fig. 6b on the dashed curve (env. 2). Note that points with a depolarization factor larger than unity are more abundant in Fig. 6b, since the envelope used represents the lowest possible one in Fig. 3c that is barely compatible with the instru-

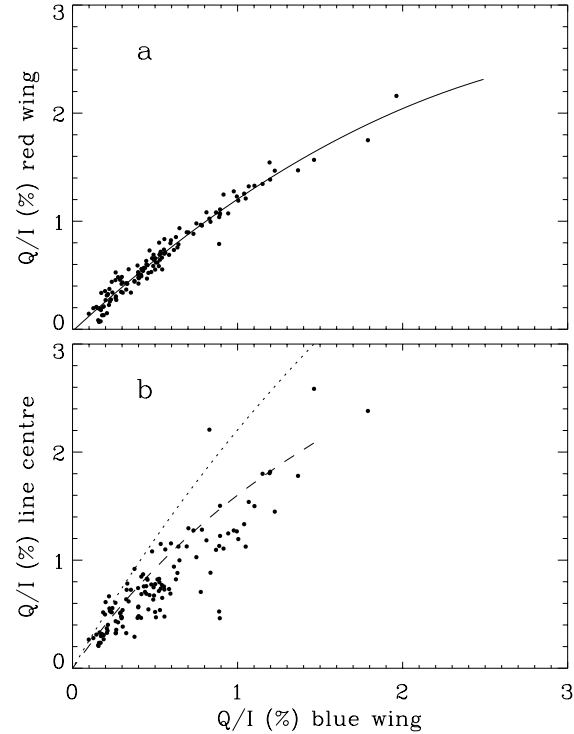


Fig. 4a and b. Relations between the polarization amplitudes in **a** the red and blue line wings, and **b** the line center and blue wing. The solid curve in **a** is a second-order polynomial fit to the data. The dotted and dashed curves in **b** have been derived from the corresponding dotted and dashed envelope curves in Fig. 3c when combined with the fit curve for the blue wing in Fig. 3a.

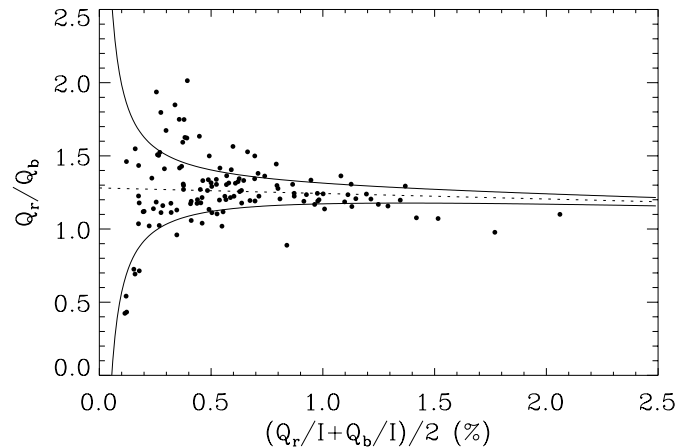


Fig. 5. Ratio between the polarization amplitudes in the red and blue line wings as a function of their mean value. The dashed line is a slightly slanted linear fit to the data. The solid curves are obtained if we add or subtract the standard deviation in the Q_r/Q_b ratio, derived from the scatter of 0.075% of the points in Fig. 4a around the polynomial fit.

mental noise. For 90° scattering (approximating observations at the extreme limb, i.e., at $\mu = 0$) ratios larger than unity are unphysical and must be due to noise, but for larger μ values ratios somewhat larger than unity are allowed (cf. the histograms in Fig. 11 below).

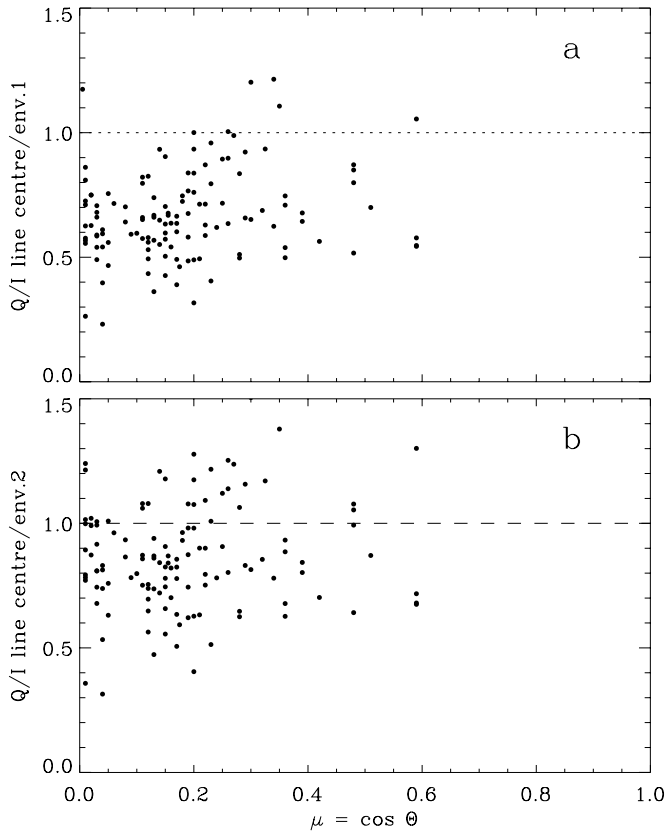


Fig. 6a and b. Ratio between the observed Q/I polarization amplitudes at line center and the corresponding Q/I envelope values, obtained as the ratio between the points in Fig. 4b and the dotted (env. 1) and dashed (env. 2) curves. The envelopes represent the values of the line center Q/I that we would have in the absence of magnetic fields.

4.3. Hanle rotation and its relation to the depolarization

In the absence of magnetic fields Stokes U is zero for symmetry reasons. It becomes non-zero when there is Hanle rotation of the plane of linear polarization. Fig. 7a shows the absolute value of the U/I amplitude at line center as a function of μ . For comparison the Q/I line-center envelopes from Fig. 3c are plotted as the dotted (env. 1) and dashed (env. 2) curves. In Fig. 7b we have plotted $|U|/Q$ (which equals $|\tan 2\beta|$, where β is the rotation angle) vs. μ . We notice that there is no systematic CLV trend for $|U|/I$ or $|U|/Q$. The occurrence of Hanle rotation depends on the local magnetic field present, not directly on μ .

To explore the relation between Hanle rotation and depolarization we have in Fig. 8a and b plotted $|U|/I$ (which is a measure of the Hanle rotation) normalized to the Q/I disk-center envelope (i.e., the ratio between the points and the curves in Fig. 7a) vs. the amount of Hanle depolarization, represented by $1 - (Q/I)/\text{env.}$ (i.e., one minus the values in Fig. 6a and b), with one diagram for each envelope choice. The error bars are based on an error of 0.075 % in U/I (cf. Sect. 4.2). To get a better feeling for the expected appearance of such a diagram we can be guided by the following theoretical considerations:

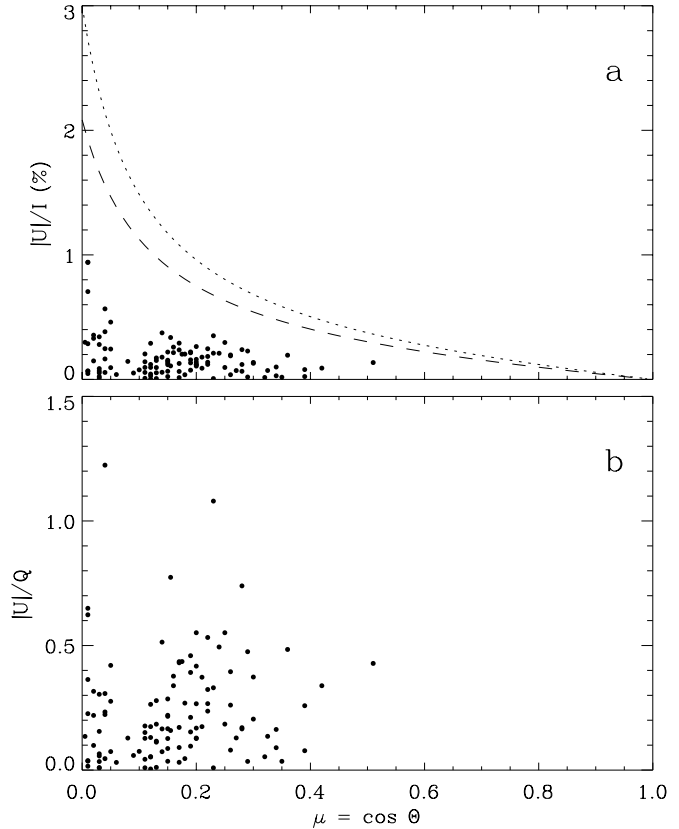


Fig. 7a and b. Center-to-limb behavior of the Stokes U amplitude in the line core. **a** The degree of polarization $|U|/I$. The dotted and dashed curves are the same Q/I line center envelope curves that were plotted in Fig. 3c. **b** The $|U|/Q$ ratio, which equals $|\tan 2\beta|$, where β is the Hanle rotation angle.

For mathematical simplicity we consider the case of single 90° scattering, as if the Sun had extreme limb darkening (such that all illumination of the scattering particles comes from the disk center), and we would be observing at the extreme limb. Due to moderate limb darkening and observations inside the limb the actual polarization amplitudes will of course be much smaller, but since we normalize all our U/I and Q/I values in Fig. 8a and b in terms of the Q/I line center envelopes, the amplitude scaling factors (due to the actual limb darkening or μ position) divide out to first order. The 90° single scattering case therefore still provides useful insight into the behavior of the normalized data. Note, however, that smaller scattering angles (corresponding to observations at larger μ values) give different distributions of the Q and U values, something that will be discussed more in connection with the histograms in Fig. 11 below.

Maximum Hanle rotation occurs when the magnetic field is directed along the line of sight, which is horizontal to the solar surface at the extreme limb. Since the for us relevant canopy magnetic fields are nearly horizontal, we will restrict our considerations here to the case of horizontal fields at the extreme limb. Then the field direction is characterized by the single parameter χ_B , the azimuth angle counted counter-clockwise from

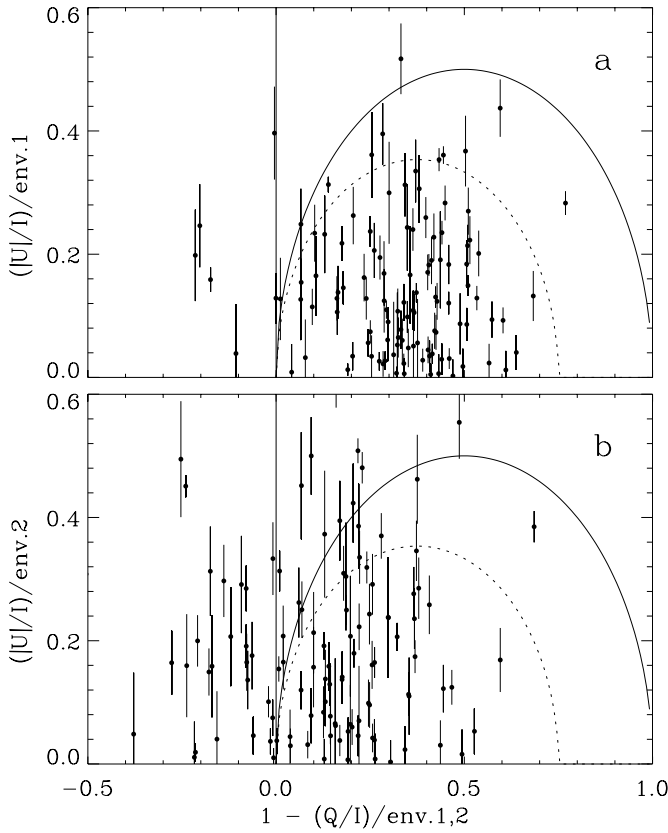


Fig. 8a and b. Relation between the Hanle rotation and depolarization effects. On the horizontal axis is $x = 1 - (Q/I)/\text{env.}$, where $(Q/I)/\text{env.}$ is obtained from the upper (env. 1) and lower (env. 2) diagrams of Fig. 6a and b. On the vertical axis is plotted $y = (|U|/I)/\text{env.}$, obtained from Fig. 7a as the ratio between the points and the two envelope curves. x is proportional to the amount of Hanle depolarization. The solid and dotted lines represent analytical curves obtained from idealized single scattering theory using the weak-field Hanle phase matrix. They are given by Eqs. (8) and (9), respectively. We expect all points to fall below the solid line, but because of noise and inadequate choice of the Q/I envelope, the data spread outside this region, in particular in the lower diagram (based on env. 2).

the direction towards the observer. The magnetic field strength is contained in the Hanle rotation angle α_2 , where

$$\tan \alpha_K = \frac{K g_u \omega_L}{\gamma_N + \gamma_c/2}, \quad (2)$$

where K can be 1 or 2 (cf. Stenflo 1994, p. 212). g_u is the Landé factor of the upper level, ω_L the Larmor precession frequency (which is proportional to the magnetic field strength), γ_N the natural, radiative damping width, and γ_c the damping width due to elastic collisions.

The polarizability of a scattering transition is as usual represented by the factor W_2 , the fraction of scattering processes that occur as classical dipole scattering (while the remaining fraction occurs like isotropic, unpolarized scattering). For the Sr II 4078 Å line $W_2 = 0.5$, for Ca I 4227 Å it is unity. Then, according to Stenflo (1994, p. 92), the scattering of incident

unpolarized radiation gives

$$\begin{aligned} Q &= \frac{3}{8} W_2 [\sin^2 \chi_B + (1 + \cos^2 \chi_B) \cos^2 \alpha_2], \\ U &= \frac{3}{8} W_2 \cos \chi_B \sin 2\alpha_2, \end{aligned} \quad (3)$$

where we have rotated the Stokes coordinate system by 90° with respect to that used in Stenflo (1994, p. 92), so that Stokes Q is defined to be positive in the direction parallel to the solar limb. In contrast to Q and U , Stokes I is largely formed by non-scattering processes which do not need to be specified here.

We get maximum Q polarization in the absence of magnetic fields, i.e., for $\alpha_2 = 0$. Thus

$$Q_{\max} = \frac{3}{4} W_2. \quad (4)$$

On the other hand, what we in our figures have called env. (the Q/I envelope) is the same as Q/I in the absence of magnetic fields:

$$Q_{\max}/I = \text{env.} \quad (5)$$

The x and y axis in Fig. 8a and b represent

$$\begin{aligned} x &= 1 - (Q/I)/\text{env.} \\ y &= (|U|/I)/\text{env.} \end{aligned} \quad (6)$$

According to Eqs. (3)–(6)

$$\begin{aligned} x &= \frac{1}{2}(1 + \cos^2 \chi_B) \sin^2 \alpha_2 \\ y &= \frac{1}{2} |\cos \chi_B \sin 2\alpha_2|. \end{aligned} \quad (7)$$

The maximum value of y (Hanle rotation) possible is obtained when $\chi_B = 0$. In this case we find from Eq. (7) the following relation between x and y :

$$y = \sqrt{x(1-x)}. \quad (8)$$

This relation is plotted as the solid curves in Fig. 8a and b. For reference, as an intermediate case, we plot the corresponding relation obtained for $\chi_B = 45^\circ$,

$$y = \sqrt{\frac{2}{3}x(1 - \frac{4}{3}x)}, \quad (9)$$

as the dotted curves in Fig. 8a and b. When $\chi_B = 90^\circ$ (magnetic field perpendicular to the line of sight), $y = 0$, i.e., the Hanle rotation vanishes.

We have plotted all the data points in Fig. 8a and b, also those with negative x values. Ideally, without instrumental scatter, all points should fall inside the area bounded by the solid curve in the case of 90° scattering (observations at $\mu = 0$), but they spread into the outside region, either because of noise or from contributions from larger μ values (for which negative x values are allowed), or because the non-magnetic Q/I envelope in Fig. 3c was chosen too low. The large spread in Fig. 8b suggests that env. 2 (dashed curve in Fig. 3c) was chosen too low, and that env. 1 (dotted curve in Fig. 3c) is to be preferred.

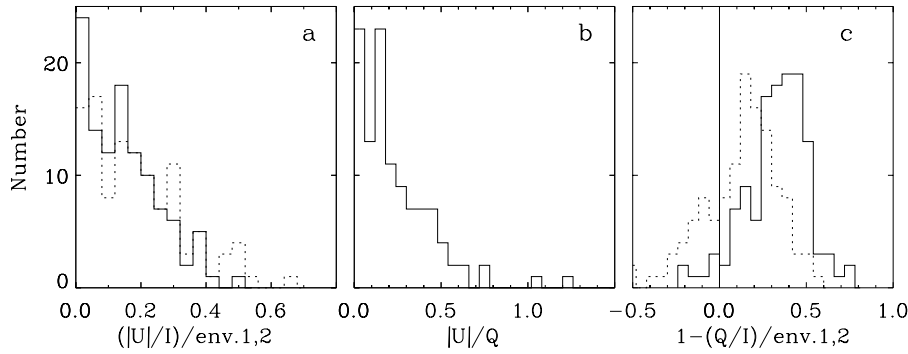


Fig. 9a–c. Histograms showing the distributions of the observational data. The solid lines in **a** and **c** are based on the use of env. 1, the dotted lines on env. 2. Panel **a** represents the distribution of the y values in Fig. 8a and b, panel **c** the distribution of the x values in Fig. 8a and b, while panel **b** gives the distribution of the points in Fig. 7b.

4.4. Histograms of the Hanle effect

The statistical distributions of the data can be expressed in the form of different “Hanle histograms”, which may be compared with theoretical histograms based on various models. Such a comparison would then allow us to gain information on the actual distribution of the magnetic field. Our empirical histograms are given in Fig. 9a–c, in which the solid lines are based on env. 1, the dotted lines on env. 2. Fig. 9a gives the distribution of the $|U|/I$ polarization expressed in units of the Q/I non-magnetic envelope, which is the parameter that was used as the y axis in Fig. 8a and b. Fig. 9b gives the distribution of the ratio $|U|/Q$, which equals $|\tan 2\beta|$, where β is the Hanle rotation angle (cf. Stenflo 1994, p. 92). The maximum at $|U|/Q = 0.15$ thus corresponds to a rotation angle $\beta \approx 4^\circ$. Note that the values of β do not depend on the choice of Q/I envelope.

Fig. 9c gives the relative amount of Hanle depolarization, $1 - (Q/I)/\text{env.}$, which was used as the x axis in Fig. 8a and b. We notice that the “spill-over” of the distribution into the negative domain is large for env. 2, as we saw in Fig. 8b, which again suggests that env. 1 is to be preferred (see however Fig. 11 below).

The observed Hanle histograms can be understood as complex mappings of the distribution of magnetic field vectors with respect to both direction and magnitude. It is in principle conceivable to invert this problem and use the observed histograms to derive the properties of the magnetic-field distributions. As such an undertaking would be far beyond the scope of the present paper, we here limit ourselves to compute theoretical histograms for a few selected special cases, which provides insight into the problem and indicates what kind of field distributions and parameter ranges that would be required to be compatible with the observed histograms.

To compute such theoretical histograms we make use of the general, weak-field Hanle phase matrix that Landi Degl’Innocenti (1988) has given in analytical form for arbitrary scattering geometries and magnetic field vectors. As before we consider a single scattering process and assume that the incident radiation is unpolarized and along the vertical direction. Since the resulting histograms depend on the scattering angle we will compute a set of histograms for two different values of the scattering angle, 90° (corresponding to $\mu = 0.0$) and 60° (corresponding to $\mu = 0.5$). Almost all our observations fall between these two extreme values. As we do not use a limb-

darkening function, the polarization scale will be wrong, but this scale factor divides out when we normalize the polarization data with the Q/I envelope. In contrast to our discussion of Fig. 8a and b we now consider all possible azimuth angles χ_B and colatitudes θ_B (angle with respect to the vertical direction) of the magnetic field vector.

The magnetic field can thus be characterized by the three parameters θ_B , χ_B , and the Hanle angle α_2 , which is a measure of the field strength. It is however more convenient to parametrize the field strength in terms of γ_B , which is related to α_2 by

$$\tan \alpha_K = K\gamma_B \quad (10)$$

($K = 1, 2$). γ_B is proportional to the field strength B :

$$B = (B_0/k_c^{(2)})\gamma_B. \quad (11)$$

B_0 is the field strength for which the Larmor precession rate equals the spontaneous radiative decay rate of the excited state. It is thus an atomic-physics constant determined by this decay rate. For our Sr II transition it is 11.8 G. The collisional factor is

$$k_c^{(2)} = \frac{\gamma_N}{\gamma_N + \gamma_c/2}, \quad (12)$$

where γ_N and γ_c are the radiative and collisional damping constants as in Eq. (2). In the higher layers of the solar atmosphere, where Sr II is formed near the solar limb, the collision rate is low, so that $k_c^{(2)}$ is not far from unity. According to the (rather crude) estimates in Stenflo (1982) it is about 0.75 at the height of formation for Sr II. In this case

$$B \approx 15.8\gamma_B \text{ (G)}. \quad (13)$$

The rather large uncertainty in the depolarizing collision rate introduces a corresponding uncertainty in the field-strength scale. A too small collision rate leads to too small values for the derived field strengths.

We may now compute, for any combination of θ_B , χ_B , and γ_B , the values of Q and U that result from a single scattering process. These values are called Q_B and U_B . The value of Q_B in the absence of magnetic fields is denoted Q_0 . Then $|U_B|/Q_0$ represents our observed quantity $(|U|/I)/\text{env.}$, while $1 - Q_B/Q_0$ represents our observed $1 - (Q/I)/\text{env.}$

For the computation of theoretical histograms we divide the unit sphere into equal-area boxes, with one grid-point at the center of each box. The boxes have equal width in colatitude

θ_B , namely π/n , where $n = 160$. For each value of θ_B we divide the parallel circle for azimuth χ_B in $2m \sin \theta_B$ intervals, rounded to the nearest integer. m is chosen to be 153 rather than 160 so that $2m \sin \theta_B$ is almost exactly an integer when $\sin \theta_B$ is small. With this division the sphere contains 31,167 equal-area boxes. A set of new grid points is generated by a small rotation of the described grid around the polar axis. Histograms for these various grids are superposed to improve the statistics.

For each grid point and each value of the field-strength parameter γ_B we compute the values of $x_1 = |U_B|/Q_0$, $x_2 = |U_B|/Q_B$, and $x_3 = 1 - Q_B/Q_0$. The angular distribution function determines how the grid points will be weighted. We make use of two different angular distributions, previously introduced for Hanle diagnostics by Stenflo (1982): (a) An isotropic distribution, and (b) a distribution that is confined to the horizontal plane and has random azimuth angles χ_B . In the case of the horizontal distribution the whole sphere does not need to be subdivided, only the equator. We then use 32,000 intervals in χ_B . For each of the two distributions, and for each given value of γ_B , we count the number of x_i values ($i = 1, 2, 3$) that fall in different x_i intervals. This gives us the theoretical histograms for x_i . Since we are here only interested in the shapes of the histograms and not in their absolute values (which depend on the choice of x_i interval widths), we have normalized all histogram curves to their maximum value.

Let us at this point note that the computation described so far implicitly assumes that the magnetic field is spatially resolved for each recording. For most fields this is not the case, but some fields must be at least partially resolved by the observations. If this were not the case and the field distribution were random *within* each spatial resolution element, then there could be no net Hanle rotation, since the positive and negative contributions would cancel each other, so all values of U would be zero. The distribution over a range of U values (or over x_1 and x_2) is only possible for partially resolved or non-random magnetic fields. For the Hanle depolarization, however, there is no such cancellation, since it occurs with only one sign. Therefore a random field distribution inside the spatial resolution element will produce a net Hanle depolarization, the amount of which is determined by the field strength. A distribution of observed amounts of Q/I polarization may then be due to a large-scale variation of the rms field strength of a random small-scale field, rather than to a large-scale variation of a resolved field. We will come back to this issue when comparing the theoretical histograms with the observed ones.

The results of our computations (based on the assumption of spatially resolved fields) are displayed in Figs. 10 and 11. The upper halves of the figures show the results for the isotropic distribution, the lower halves for the horizontal distribution of field vectors. The solid, dashed, and dotted curves correspond to the values 1, 0.5, and 0.25, respectively, for the field-strength parameter γ_B . Note that in the lower left diagram of Fig. 10 the solid and dotted curves coincide.

For each value of γ_B only a certain range of x_i values are possible. A curve can end at its maximum value unity at one edge of its x_i range, or it can end at an intermediate value. Beyond

these end points no points can exist. Due to our normalization all curves reach unity somewhere. In the lower $|U|/Q$ panel of Fig. 10 the solid curve turns up and reaches unity only for higher x_i values outside the displayed range.

Let us now compare the theoretical histograms of Figs. 10 and 11 with the observed ones in Fig. 9a–c to see if the observations can be understood within the framework of our idealized theoretical model. The shapes of the theoretical curves look quite different from those of the observed histograms, but we have to remember that the theoretical curves have been obtained for fixed, single-valued field strengths. With a more realistic field-strength distribution we would have to make weighted averages of different shifted curves, like the solid, dashed, and dotted ones in Figs. 10 and 11, which would result in rounded distributions similar to the observed ones in Fig. 9a–c. A refined treatment should also account for the μ distribution of the observations.

The range covered by the observational histogram for the Hanle depolarization $1 - (Q/I)/\text{env.}$ (Fig. 9c) is best represented by the theoretical dashed curves in Figs. 10 and 11, for $\gamma_B = 0.5$. According to Eq. (13) this correspondence requires the field strengths to be about 5–10 G.

Note that the distributions of the depolarization x_3 spill over more and more into the negative regime as the value of μ increases, as shown by the panels to the right in Fig. 11. Therefore the data points that fall into this regime need not all be due to noise, since some spill-over is actually expected. This μ dependence of the histograms needs to be accounted for in future more detailed quantitative interpretations. We also have to deal with another quite fundamental interpretational problem, namely the finite spatial resolution of the observations.

The observational histograms for the Hanle rotation (Figs. 9a and 9b) spread over a considerably smaller range of $(|U|/I)/\text{env.}$ and $|U|/Q$ (x_1 and x_2) values than would be expected from a 5–10 G field according to the corresponding diagrams in Figs. 10 and 11. This inconsistency between Hanle depolarization and rotation indicates that the underlying assumption for the theoretical histograms, namely that the magnetic fields are spatially resolved (homogeneous within each solar region to which an observed spectrum corresponds), is not correct.

From our previous knowledge about the structure of solar magnetic fields we know that most of the magnetic flux is indeed spatially unresolved. On the other hand, if all the unresolved flux had no net orientation when averaged over the spatial resolution element, then no non-zero values for the Hanle rotation could occur, all U values would be zero, and the histograms in Figs. 9a and b would just have a peak at $x_{1,2} = 0$, with some spread due to observational noise. The circumstance that the spread is much larger than the noise indicates that large-scale orientations of the field which do not average out over small scales are indeed present. Such a large-scale field with a strength on the order of 5–10 G can have contributions either from a global component of the Sun's general magnetic field, or from canopy fields, which have their sources in the supergranular network and spread nearly horizontally in the lower chromosphere over the supergranular cells (cf. Giovanelli 1980; Solanki & Steiner

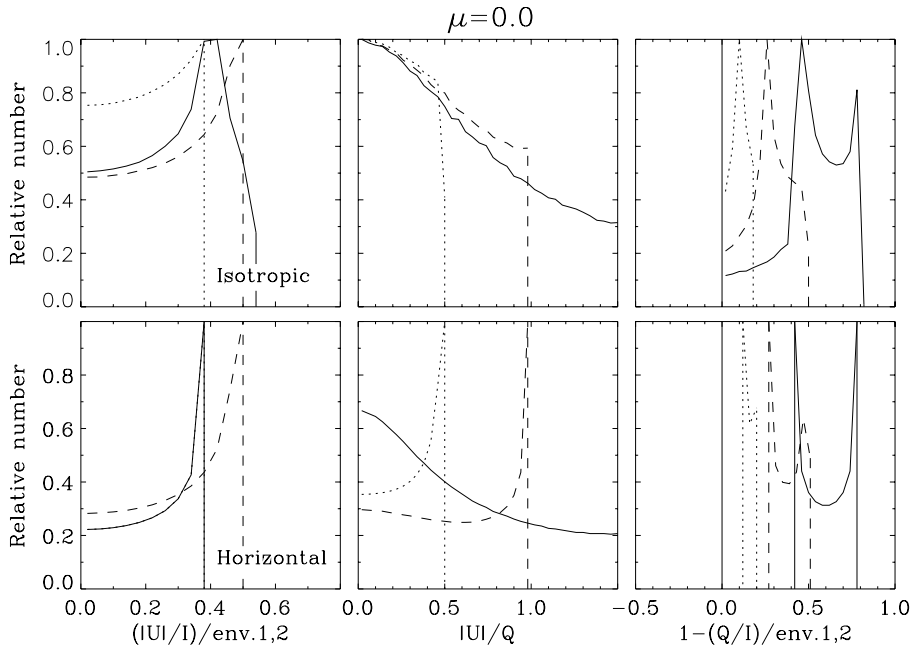


Fig. 10. Theoretical histograms for the same parameters as determined observationally in Fig. 9a–c. The curves are based on an idealized single-scattering model assuming spatially resolved magnetic fields and two different angular distributions of field vectors, an isotropic (upper panels) and a random horizontal (lower panels) distribution. 90° scattering is assumed, corresponding to observations at the extreme limb ($\mu = 0$). The solid, dashed and dotted curves correspond to the values 1.0, 0.5, and 0.25 for the field-strength parameter γ_B that is related to the field strength B via Eq. 13). For details, see the text.

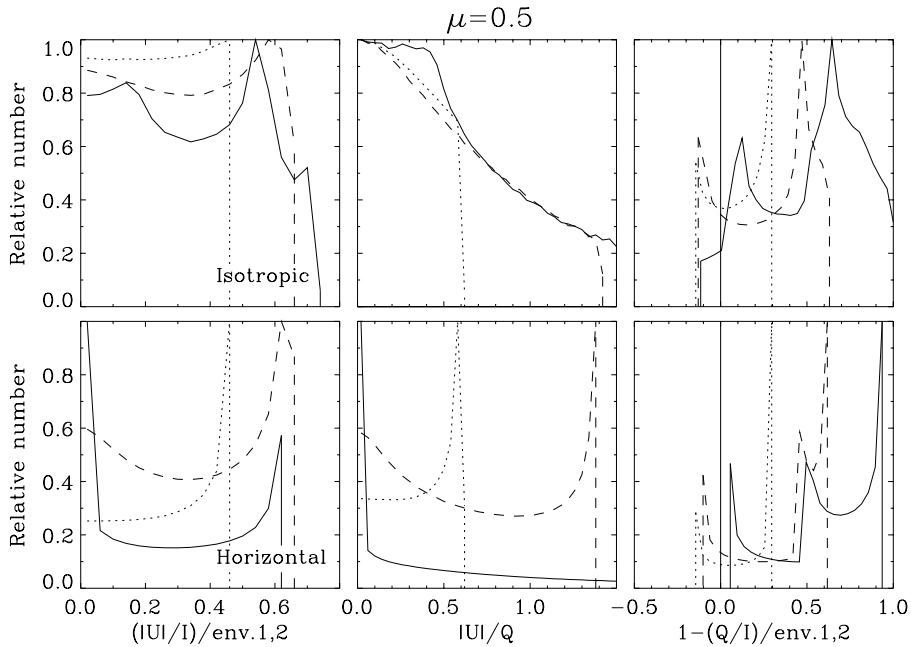


Fig. 11. Same as Fig. 10, except that the scattering angle is assumed to be 60° , corresponding to observations at $\mu = 0.5$.

1990). The canopy fields can be expected to statistically obey a nearly horizontal, random distribution of field vectors with a spatial coherence over scales comparable to the supergranulation (30 Mm), while the global field component can be coherent over larger scales.

On a much smaller, even subtelescopic or optically thin scale, we can expect the presence of an isotropically distributed turbulent field, which reveals itself through Hanle depolarization but not through Hanle rotation (Stenflo 1982, 1994; Faurobert-Scholl 1993; Faurobert-Scholl et al. 1995). If such a field had a single-valued field strength, it would in the Hanle depolarization diagram (Fig. 9c) for each given μ value contribute to a peak located at a non-zero value of the depolarization x_3 . A

field-strength and μ distribution would widen the peak, to make it look more like the observed distribution in Fig. 9c. Again, for the depolarization peak to be located at the observed place the field strengths would need to be around 5–10 G, as we will derive more directly in the next subsection. However, regardless of field strength, the turbulent field would try to make the Hanle rotation histograms in Figs. 9a and b peak around zero x_1 and x_2 . If we now to this small-scale turbulent field add a large-scale field (like a canopy field or a global field) with net large-scale field orientations, then we see that with a proper combination of these two kinds of fields (small and large scale), we may build Hanle rotation histograms that look like those of Figs. 9a and b. The apparent inconsistency between the histograms for the

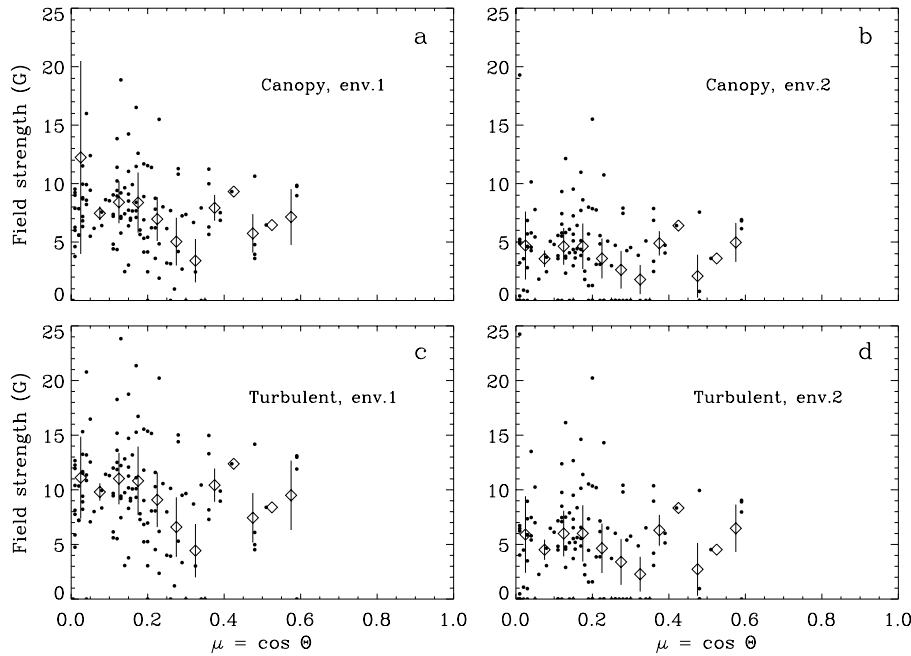


Fig. 12a–d. Magnetic field strengths derived from the observed Hanle depolarization in Q/I with the assumption that the fields are spatially unresolved, and that we average over a complete angular distribution of field vectors within each spatial resolution element. The figure has been obtained by converting the data in Fig. 6a and b, which are supposed to represent the Hanle depolarization factor k_H , into field strengths via Eq. (14) for isotropic (lower panels) and random horizontal (upper panels) field distributions. The diamonds with error bars represent averages and standard deviations of the data points within μ intervals of width 0.05.

Hanle rotation and depolarization can indeed be resolved if we have a mixture of contributions from resolved and unresolved fields.

This rather involved discussion shows that with the present data no unique interpretation is possible, but that the observed histograms can be understood in terms of plausible magnetic-field scenarios. These scenarios would be differently constrained by other lines with different sensitivities to the Hanle effect. It should therefore be possible to greatly reduce the ambiguity in the interpretations by making use of the differential Hanle effect for combinations of spectral lines, and of course also by combining Hanle diagnostics with high spatial resolution.

4.5. Field strengths from the observed Hanle depolarization

We will now adopt the assumption (contrary to the assumption on which the theoretical histograms in Figs. 10 and 11 were based) that the fundamental magnetic structures are spatially unresolved, and that we average over a complete angular distribution of field vectors within each spatial resolution element. The Hanle depolarization factor k_H that results from this averaging is then identified with our observed depolarization factors $(Q/I)/\text{env}$. The factor k_H can be obtained in analytical form for various angular distributions, as has been shown by Stenflo (1982) for a horizontal (canopy-type) random distribution, and for an isotropic (turbulent-type) distribution. The resulting expressions obtained by averaging the weak-field Hanle phase matrix over these two types of angular distributions are

$$\begin{aligned} k_H^{\text{turbulent}} &= 1 - 0.4(\sin^2 \alpha_1 + \sin^2 \alpha_2), \\ k_H^{\text{canopy}} &= 1 - 0.75 \sin^2 \alpha_2. \end{aligned} \quad (14)$$

The Hanle mixing angles α_1 and α_2 have been given by Eqs. (2) and (10)–(13), which allow us to translate the quantity $(Q/I)/\text{env}$ into field strength.

We have thus taken all the values in Fig. 6a and b (after the values > 1 have been set $= 1$, since to be compatible with Eq. (14) such values are unphysical and must be due to noise) and converted them with the above equations, to obtain the four diagrams in Fig. 12a–d. In these diagrams we have also determined the mean value and standard deviation of the points within μ intervals of width 0.05 and plotted them as diamonds with error bars. Note that the converted “unphysical” values enter into the diagrams with $B = 0$ and also contribute to the derived means and error bars.

We notice in Fig. 12a–d that the diagrams based on env. 1 (the preferred envelope) gives field strengths that are systematically somewhat larger than those based on env. 2, which produces many more “unphysical” points. The field strengths obtained with env. 2 can be regarded as a lower limit to the field strengths that would be obtained if a “true” non-magnetic Q/I envelope could be used. The assumption of an isotropic, turbulent field distribution results in somewhat larger field strengths than when a horizontal, canopy-type angular distribution is used, but these differences are smaller than the scatter of the points. The typical mean field strengths are 5–10 G, the same as we estimated from the Hanle histograms in Sect. 4.4. These results are consistent with and similar to those of Paper I for the Ca I 4227 Å line. The Sr II line gives on average 30% lower values, but due to the uncertainties in the rate of depolarizing collisions, this difference cannot be regarded as very significant.

4.6. Profile shape of the Hanle effect

One fundamental and non-trivial property of the Hanle effect is that it is present in the Doppler core but absent in the line

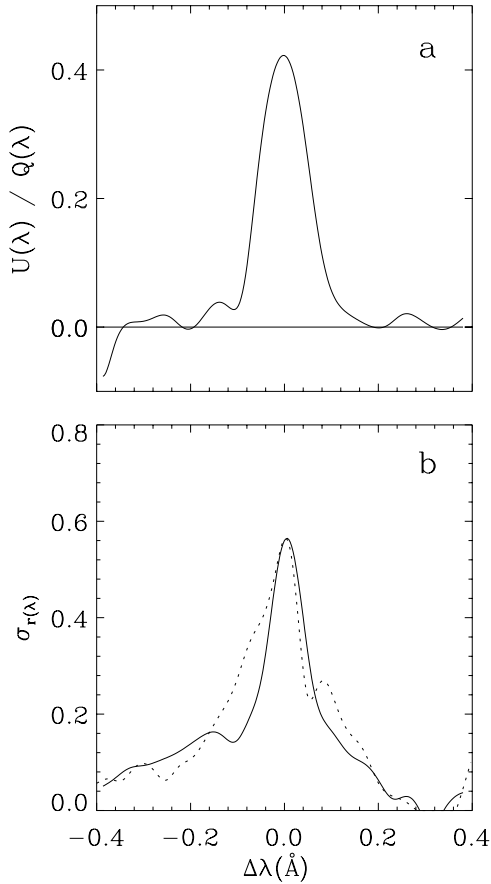


Fig. 13a and b. Empirical profiles for the Hanle efficiency, showing how the Hanle effect is active in the line core but vanishes in the line wings. **a** Profile of the Hanle rotation efficiency, obtained as the ratio between the dotted (U/I) and solid (Q/I) curves in Fig. 1c. **b** Profile of the Hanle depolarization efficiency, represented by the standard deviation or scatter $\sigma_{r(\lambda)}$ of the observed values of $r(\lambda)$, where r is defined by Eq. (15). The solid curve has been derived from the present Sr II data, the dotted curve from the Ca I data of Paper I. To facilitate the comparison between the different profiles, the Ca I curve has been rescaled, and the zero points for the two curves have been slightly shifted, as described in the text.

wings. There must therefore be a wavelength variation of the Hanle efficiency with a transition from core to wings, i.e., the Hanle efficiency has a certain profile shape. With our extensive statistical material of polarized line profiles with various amounts of Hanle rotation and depolarization, we are now for the first time in a position to determine empirically the profile shape of the Hanle effect.

One very direct way to do this is to simply form the ratio between the mean U/I and Q/I profiles (the dotted and solid curves in Fig. 1c). As U/Q equals $\tan 2\beta$, where β is the Hanle rotation angle, the resulting ratio profile, which is plotted in Fig. 13a, represents the profile of the Hanle rotation effect. Its width and shape are in full accord with theoretical expectations, although a detailed quantitative comparison with theory is outside the scope of the present paper.

The general profile behavior (the requirement that U should be zero in the far wings) has however been assumed by us in the procedure for the elimination of the instrumental $Q \rightarrow U$ cross talk. It would therefore be good to have a confirmation of this profile shape independent of this assumption.

Such an independent determination can be made by using the statistical Hanle depolarization information in the Q/I profiles alone, without reference to U . The procedure is the following: Using the value of Q/I at a fixed wavelength λ_{ref} in the far line wings as a reference, we form the ratio

$$r(\lambda) = \frac{Q(\lambda)/I(\lambda)}{Q(\lambda_{\text{ref}})/I(\lambda_{\text{ref}})} \quad (15)$$

as a function of wavelength λ . The choice of λ_{ref} is not critical (although it should be chosen in an unblended portion of the line wing), it mainly determines the unit or scale for r , but this scale factor is immaterial anyway, since we are only interested in the profile shape.

For each given value of λ the different recordings will give different values of r . We interpret this variation in the r value as being due to the varying Hanle depolarization in Q/I . The variation will be larger when the Hanle depolarization efficiency is larger. We therefore determine, for each given λ , the standard deviation $\sigma_{r(\lambda)}$ in the values of $r(\lambda)$ for all our Q/I recordings. $\sigma_{r(\lambda)}$ should be proportional to the amount of Hanle depolarization.

This kind of analysis is also possible for our previous Ca I 4227 Å Q/I line profiles that were used in Paper I. In Fig. 13b we plot the results for $\sigma_{r(\lambda)}$ for both lines: The solid curve for Sr II, the dotted for Ca I. Since the normalization of $r(\lambda)$ (through the choice of λ_{ref}) is different for Sr II and Ca I, we have multiplied the $\sigma_{r(\lambda)}$ values for Ca I by the constant factor 2.3 to make the profile scales comparable for the two spectral lines.

Since $\sigma_{r(\lambda)}$ is a standard deviation, it can never be negative, and it reaches zero by definition at the chosen reference wavelength λ_{ref} (in the right portion of Fig. 13b). Noise contributes to σ with only one sign (positive) and causes the far wings to be elevated above the zero level (except at λ_{ref}). To bring this elevated noise level down we have subtracted a constant from the $\sigma_{r(\lambda)}$ values. We have chosen this constant to be 0.065 for Sr II and somewhat less, 0.046, for the scaled Ca I values, since the noise level was smaller for the Ca I data.

A comparison between the profile shapes and widths of the different curves shows that there is general agreement, both between Sr II and Ca I, and between $\sigma_{r(\lambda)}$ and $U(\lambda)/Q(\lambda)$. This agreement further confirms the Hanle interpretation of our data, and we now have the first empirical Hanle efficiency profiles, which later may be compared with corresponding theoretical profiles. We note in particular the good agreement between the independently determined Hanle rotation and depolarization profiles.

5. Conclusions

In the present paper we have for the Sr II 4078 Å line applied the same observational and analysis techniques that we used in Paper I for the Ca I 4227 Å line, but we have also significantly extended and refined the Hanle diagnostics. From the observational point of view the main new features are the recording of not only Stokes I and Q , but also of Stokes U , which allows us to detect the Hanle rotation of the plane of polarization, and the use of a rapidly tilting servo glass plate to stabilize the solar limb with respect to image motions. From the analysis point of view the main new highlights are the introduction of Hanle histograms for the diagnostics of magnetic field distributions, and the first empirical determination of the profile shape of the Hanle efficiency, showing the way in which the Hanle rotation and depolarization effects vary when we go from the line core to the wings.

In the areas where our analysis methods have been the same as those of Paper I, we find that the scattering polarization in the Sr II and Ca I lines behave very much the same with respect to the Hanle effect, although these lines have different atomic structures (and intrinsic polarizabilities) and polarized line shapes. Assuming spatially unresolved angular field distributions we derive from the Sr II analysis typical field strengths of 5–10 G, similar to those derived from the Ca I data. These field strengths are confirmed by the shapes and widths of our Hanle histograms, which in addition provide information on the strengths and angular distributions of spatially resolved fields. Such fields reveal themselves by producing a non-zero Stokes U signature, which can only occur if there are resolved, net large-scale orientations of the field, e.g. from a global component of the Sun's magnetic field, or from magnetic canopies across the supergranulation cells. The consistency between the various analysis methods and results, and the derived Hanle efficiency profile shapes, confirm the Hanle interpretations of the data and put the astrophysical use of the Hanle effect on firmer ground.

Hanle histograms offer us a new potentially powerful tool to derive detailed information on the distributions of magnetic field strengths and orientations. We have to be aware, however, that both spatially resolved and unresolved fields (with field distributions within the resolution element) contribute to these observed histograms. With our present data set it is not possible to unambiguously separate all the different kinds of contributions from each other. Such ambiguities can be greatly reduced and hopefully eliminated by using differential Hanle diagnostics, i.e., by comparing the scattering polarization in certain combinations of spectral lines with different sensitivities to the Hanle effect, a new technique that has been explored by Stenflo et al. (1998). This will allow additional observational constraints to be added, such that a unique inversion of the Hanle problem may become possible. Observationally we need to develop better methods to eliminate the instrumental polarization cross talk, which in our case has its probably main source in the entrance window of the telescope. We also need to include Stokes V for full vector polarimetry to combine the diagnostic powers of the Zeeman and

Hanle effect and access a broader parameter domain of solar magnetism.

Acknowledgements. The system to stabilize the solar limb with a tilting glass plate was proposed by E. Wiehr (Göttingen) and constructed as part of a Masters thesis by D. Thomas (Wiesbaden). V. Bommier (Meudon) made us aware of the significant μ dependence of the Hanle histograms and led us to discover mistakes in the computer program used to calculate them. We are grateful for the financial support that has been provided by the canton of Ticino, the city of Locarno, and the ETH Zurich.

References

- Bianda, M., Solanki, S.K., Stenflo, J.O., 1998, A&A 331, 760 (Paper I)
 Faurobert-Scholl, M., 1993, A&A 268, 765
 Faurobert-Scholl, M., Feautrier, N., Machefert, F., Petrovay, K., Spielfiedel, A., 1995, A&A 298, 289
 Giovanelli, R.G., 1980, Solar Phys. 68, 49
 Landi Degl'Innocenti, E., 1988, A&A 192, 374
 Landi Degl'Innocenti, E., 1998, Nature 392, 256
 Pierce, A.K., Slaughter, C.D., 1977, Solar Phys. 51, 25
 Povel, H.P., 1995, Optical Engineering 34, 1870
 Semel, M., 1995. In: 3D Spectroscopic Methods in Astronomy, Comte, G., Marcellin, M. (eds.), ASP Conf. Ser., vol. 71, p. 340
 Semel, M., Donati, J.-F., Rees, D.E., 1993, A&A 278, 231
 Solanki, S.K., Steiner, O., 1990, A&A 234, 519
 Stenflo, J.O., 1982, Solar Phys. 80, 209
 Stenflo, J.O., 1994, Solar Magnetic Fields – Polarized Radiation Diagnostics. Kluwer, Dordrecht
 Stenflo, J.O., Baur, T.G., Elmore, D.F., 1980, A&A 84, 60
 Stenflo, J.O., Twerenbold, D., Harvey, J.W., 1983a, A&AS 52, 161
 Stenflo, J.O., Twerenbold, D., Harvey, J.W., Brault, J.W., 1983b, A&AS 54, 505
 Stenflo, J.O., Bianda, M., Keller, C.U., Solanki, S.K., 1997, A&A 322, 985
 Stenflo, J.O., Keller, C.U., Gandorfer, A., 1998, A&A 329, 319
 Sütterlin, P., Wiehr, E., Bianda, M., Küveler, G., 1997, A&A 321, 921